PHOTOACTIVE THIN FILM SEMICONDUCTING IRON PYRITE PREPARED BY SULFURIZATION OF IRON OXIDES

G. SMESTAD *, A. ENNAOUI, S. FIECHTER, H. TRIBUTSCH, W.K. HOFMANN, M. BIRKHOLZ

Hahn Meitner Institute Berlin, Abteilungen Solare Energetik und Materialforschung, Glienicker Strasse 100, D-1000 Berlin 39, Germany

and

W. KAUTEK

Laboratory for Chemical Surface Technologies, Federal Institute for Materials Research and Testing (BAM), Unter den Eichen 87, D-1000 Berlin 45, Germany

Photoactive iron pyrite (FeS_2) thin film layers have been synthesized by a simple method involving the reaction of Fe_3O_4 or Fe_2O_3 with elemental sulfur. The films were formed on a variety of different substrate materials by converting or sulfurizing iron oxide layers. The subsequent sulfur treatment of the oxide layers consisted of exposure of the films to gaseous sulfur in open or closed ampules at 350°C for 0.5–2 h. The morphology, composition and photoactivity of the films produced were checked using X-ray diffraction, X-ray photoelectron spectroscopy (ESCA), optical absorption, steady state and transient photoconductivity. The best films showed good crystallinity and purity with concurrent photoconductivity and photoelectrochemical response. The ability of this technique to produce photoactive material can be explained by interpretation of the Gibbs ternary phase diagram for the Fe–O–S system, and may be related to the production of photoactive pyrite in nature. A discussion is made as to the future improvement of the solar cell response by proper optimization of geometric and configurational properties.

1. Introduction

1.1. Background

One of the challenges for the future development of renewable energy from the sun is to find techniques capable of producing photoactive semiconductive materials using inexpensive and reliable techniques. By virtue of the abundance of its constituent elements, and the material's properties (indirect band gap $E_g = 0.9$–1.0 eV, absorption coefficient, $\alpha = 10^5$ cm^{-1}, Hall mobility at room temperature,

---

* Hewlett Packard Company, Optoelectronics Division, 370 W. Trimble Road, San Jose, CA 95131, USA.

$\mu > 350$ cm^2/V·s, diffusion length, $L > 0.12$–1.0 μm) iron pyrite, or FeS$_2$, has seemed to be a recent candidate for solar cells [1–4]. It is also promising that for this d-transition material, the photogeneration of carriers involves non-bonding orbitals, which leads to the ability of this material to be used in a simple photoelectrochemical cell without photocorrosion [5]. Previous publications have described techniques such as chemical vapor transport, CVT, metal organic chemical vapor deposition, MOCVD, or chemical spray pyrolysis, CSP, to synthesize pyrite [6–8]. The resulting crystals or films do not represent the properties of pure pyrite due to the presence of trace amounts of conductive metallic FeS, or deviation from ideal stoichiometry. It has been postulated that a sulfur deficiency can generate a mid bandgap defect band and thus decrease the barrier height and photovoltages in pyrite solar cells [8]. In the next sections, we will present a new technique for the production of pyrite that involves a reaction pathway which can avoid the formation of sulfur deficient pyrite.

1.2. Phase diagram

The main disadvantage of preparing pyrite from the elements is that the first step in the reaction must necessarily be the formation of iron rich layers containing a phase of the type Fe$_{1-x}$S. This can be seen from the ternary phase diagram shown in fig. 1, which is calculated for equilibrium conditions using enthalpy, Gibbs free energy and heat capacity at 350°C and a pressure of 1 atmosphere. This Fe–O–S diagram is essentially the same as that proposed by Kullerud in 1957 [9]. Preparing pyrite by CVT, CSP or MOCVD in the absence of oxygen, one must pass through the FeS phase field. However, if sulfur is added to the oxides Fe$_3$O$_4$ or Fe$_2$O$_3$, one does not cross the FeS phase field. Instead, for the reaction of Fe$_2$O$_3$ and S, pyrite and SO$_2$ gas are produced, and for the reaction of Fe$_3$O$_4$ and S, pyrite and Fe$_2$O$_3$
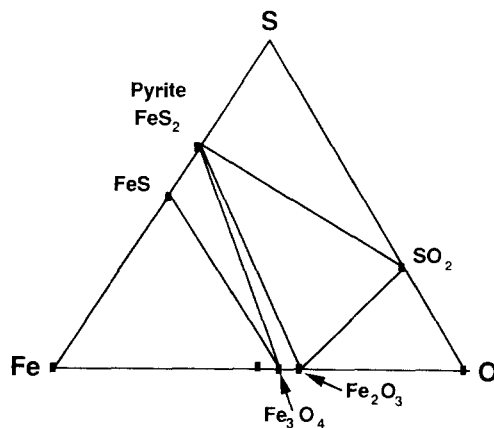
Fig. 1. Fe–O–S phase diagram. The tie lines are calculated for $T = 350$°C and a total pressure of $P = 1$ atm [9].

are formed. This synthesis technique has been suggested in the past as a mechanism of pyrite synthesis in nature, but its importance in the production of pyrite for a semiconductive solar cell has not been explored [6]. This formation process may also explain why natural photoactive single crystals of pyrite are observed from some locations (i.e. Morgul–Turkey) [1–4].

2. Experimental methods

2.1. Layer preparation

All layers were obtained by the reaction of Fe_2O_3 or Fe_3O_4 with the gases of sulfur both heated to 350°C for 0.5 to 2 h. An open system consisting of a spray apparatus [8] configuration was used to sulfurize the oxide films, or sulfurization could take place in closed quartz ampules. The two relevant reactions at this temperature are:

$$2\,Fe_2O_3(s) + 11\,S \rightleftarrows 4\,FeS_2(s) + 3\,SO_2(g), \quad \Delta G = -42.8 \text{ kcal/mol}, \tag{1}$$

$$Fe_3O_4(s) + 8\,S \rightleftarrows 3\,FeS_2(s) + 2\,SO_2(g), \quad \Delta G = -32.5 \text{ kcal/mol}. \tag{2}$$
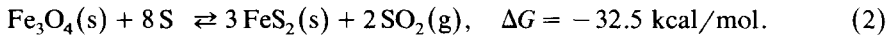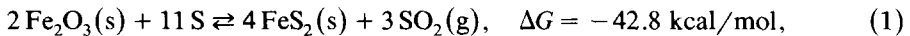
From the phase diagram, the second reaction involves Fe_2O_3 as an intermediate. The oxide layers were prepared by the evaporation of 1000 Å of iron on the substrate material, with the subsequent oxidation in a nitrogen and oxygen gas flow at 350°C. For two experiments, the oxide films were also prepared by pyrolysis of $FeCl_2$, in the case of Fe_3O_4, and $FeCl_3$, for the production of Fe_2O_3. The temperatures and apparatus are the same as used to form pyrite by CSP [8].

The evaporated layers were deposited on 0.025 mm Dupont Kapton polyimide, or on 0.55 mm transparent conductive, ITO, Schott AF45 glass. The sprayed oxide layers were deposited on AF45 glass alone. With both substrates, excellent adherence to pyrite has been observed.

2.2. Layer characterization

X-ray diffraction plots were measured in a θ–2θ coupled geometry with a Siemens D500 operating a Cu anode at 45 kV and 30 mA. A secondary graphite monochromator was used to avoid $K\beta$ lines and to reduce fluorescent scattering from the iron K edge absorption of the Cu Kα radiation, λ(Cu Kα_1) = 1.54059455 Å ±0.7 ppm [10]. Crystallite size analysis was performed with the help of the Scherrer formula [11]. This technique uses the excess broadening of the X-ray diffraction lines for the calculation of a mean diameter of coherent scattering domains. The resulting grain sizes are generally smaller than those obtained with the scanning electron microscope (SEM). A standard CeO_2 sample (NBS standard reference material 674) was measured to check the instrumental broadening due to slit settings and other geometrical conditions. This instrumental broadening was deconvoluted from the measured sample profile via a transformation to the Fourier

components space [12]. For the diffraction lines, a fit was done to the 4-parameter regular Pearson VII and 3-parameter Lorentz functions [13].

Small spot X-ray photoelectron spectra (SSXPS) were done to elucidate the chemical composition of the films. We employed a Surface Science Instruments model 206 X-probe ESCA system with a remote control Auto ESCA XYZR sample manipulator for automated sample motion. The high intensity X-ray source ($Al K\alpha_{1,2} = 1486.6$ eV) was monochromated by a quartz crystal diffraction element, and could be focused to a user selectable X-ray spot size between 150 and 1000 μm. The electron energy analyzer was of the $180°$ spherical electrostatic type fitted with a 128-channel, pulse counting, position sensitive resistance, anode encoder detector. Data acquisition and spectra deconvolution was done on a Hewlett Packard 9000 series 200 desktop computer system.

Time-resolved (transient) microwave photoconductivity, TRMC, was done to probe the film's photoresponse and carrier lifetimes without the use of electrical contacts. A description of this technique can be found in the literature [14,15]. A commercial system is also available from Phoenicon in Berlin [16]. Steady state photoconductivity was performed using the four-point probe set up. Four contacts were made by painting Au epoxy stripes, 1 mm wide by 5 mm long, on the surface of the film, and were then verified for ohmic response. A constant current is then passed through the outer probes and the voltage is measured between the irradiated inner probes. The photoresponse signal was determined by a lock-in amplifier synchronized with the chopped light beam. The monochromatic light was selected using a Kratos GM 252 monochromator with proper optical filters used to eliminate second order diffraction. The light intensity and photon flux used for normalization was measured by a calibrated pyroelectric radiometer (PK 5000). Optical absorption measurements were performed with a Bruins Instruments Omega spectrophotometer equipped with an integrating sphere. Photoelectrochemical measurements were made using pyrite deposited on ITO glass mounted as an electrode and placed in contact with an aqueous I^-/I_3^- electrolyte redox system [2].

3. Experimental results

3.1. Phase and composition

X-ray diffraction showed all pyrite lines within the measured range and some second phases, which could be assigned to unconverted iron oxide, iron or indium oxide from the conductive glass. Foreign phases and calculated mean grain sizes are shown in table 1. Films prepared by CSP as well as sulfurization of iron oxides are shown for comparison.

X-ray diffraction plots for film AE1 deposited on ITO glass, and AE3 deposited on Kapton are shown in fig. 2, where the position of the pyrite lines are indicated. Some residual ITO, In_2O_3, lines are present in AE1 due to substrate diffracted X-rays passing through the thin pyrite film. Substrate diffraction causes a broad amorphous Kapton peak for AE3. The pyrite peaks for AE3 are more intense

Table 1
X-ray diffraction analysis of some typical sulfurized and CSP [8] films (unless otherwise stated, the substrate was AF45, and pyrite lines were detected)

Film	Preparation conditions	XRD phases (other than FeS_2)	Mean grain size (nm)
SP817B	Sprayed	none	9.0
GS828B	Sulfurized on ITO	ITO	11.1
GS823	Sulfurized	Fe_3O_4	12.1
AE1	Sulfurized on ITO	Fe, ITO	7.0
AE3	Sulfurized on Kapton	none	11.8

compared with AE1 since, during the preparation of AE1, the iron coated ITO glass has not converted to oxide from top to bottom (which is later sulfurized to pyrite). This also results in a larger grain size for AE3.

Experiments were also done sulfurizing sprayed films of Fe_2O_3 and Fe_3O_4 on glass. It was found that both films converted to pure pyrite. The hematite film
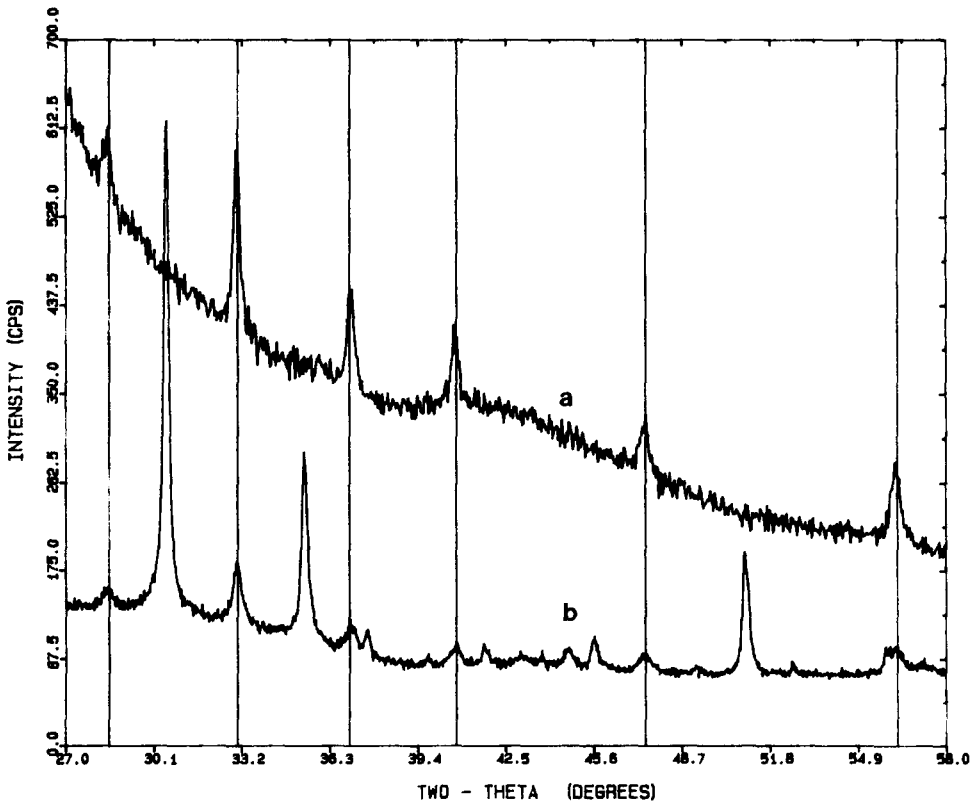
Fig. 2. X-ray diffraction of a pyrite film on (a) Kapton (AE3) and (b) ITO glass (AE1).
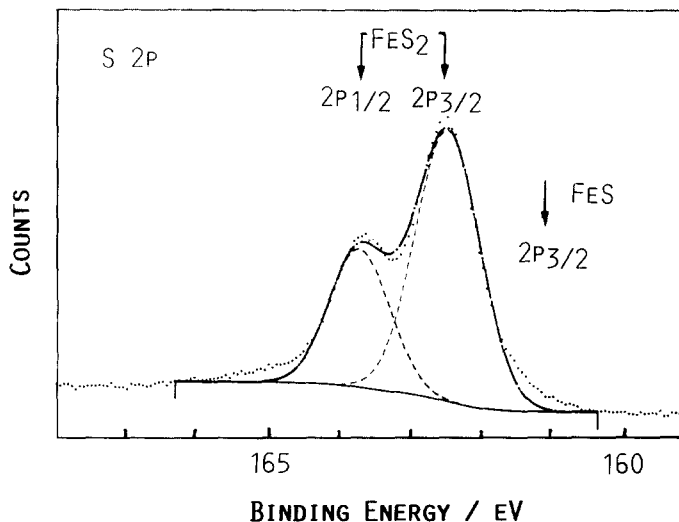
Fig. 3. Sulfur 2p XPS of sulfurized specimen on ITO after air contact at room temperature.

(Fe_2O_3) conversion was incomplete unless an excess of sulfur was used. This may be explained by the phase diagram (fig. 1), since more sulfur is needed to cross the FeS_2–SO_2 tie line from Fe_2O_3 than to cross the FeS_2–Fe_2O_3 line from Fe_3O_4. It can be assumed that for this reason conversion of magnetite Fe_3O_4 into pyrite was complete and took place in a shorter time.

Small spot ESCA (XPS) analysis with a spot size of 600 μm yielded three-dimensional information about elemental constituents and their bonding states in the ITO glass pyrite film. The major result is that the oxygen and sulfur treatment of the films can yield conversion to pyrite near 100%. The sulfur 2p results at 162.5 eV ($2p_{3/2}$) and 163.7 eV ($2p_{1/2}$) [17–22] in fig. 3 prove the purity of the pyrite film. The absence of FeS which should appear near 161 eV [17,18] is secured within an error of a few percent. Fig. 4 shows an iron 2p signal at 707 eV characteristic for 80 at% FeS_2 [17–19]. The remaining 20 at% occur as an iron-oxyhydroxide, $FeO_x(OH)_y$, species [17]. FeS should be expected near 710 eV [19] as indicated, but is not seen. We can show from the depth profiles of figs. 5–7 that the oxyhydride species is present only on the surface of the film, and that the bulk consists of near 100% pyrite. Depth profiling by argon ion sputtering (fig. 7) removes oxygen species such as $FeO_x(OH)_y$ and carbohydrates within 100 s at a sputter rate 0.17 nm s^{-1}. We calibrated sputter rates to Ta_2O_5. Measurements of film thickness using a step profiler agreed with the depth obtained by sputtering. Within the film depth of about 180 nm, practically pure FeS_x is found with $x = 2.2$. The deviation from 2.0 might be due to instrumental factors not calibrated to this particular case.

One can conclude that the first 180 nm consists of pure pyrite FeS_2. Beyond this layer, oxygen is successively accumulated at the cost of sulfur as the ITO interface is approached. This intermediate zone between FeS_2 and ITO comprises at least 140 nm. We are currently investigating the analogous interface on Kapton foils. Fig. 5
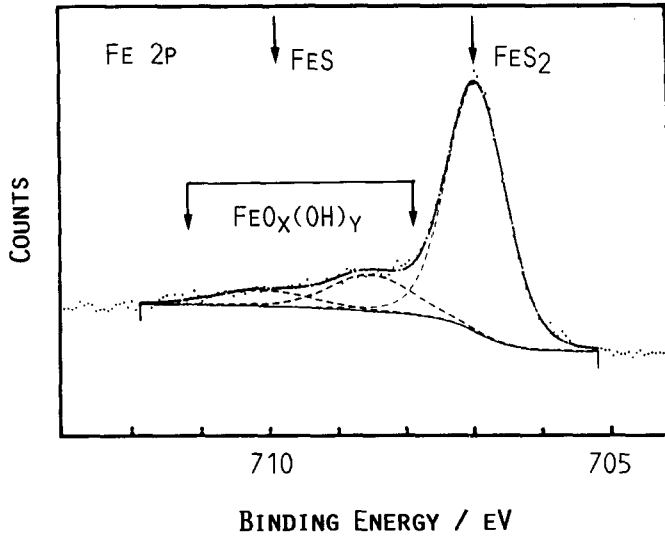
Fig. 4. Iron 2p XPS of sulfurized specimen on ITO after air contact at room temperature.

indicates the chemical shift of the sulfur 2p signal. Traces of SO_x at 168.9 eV [17] exist only in the surface. In the bulk phase, sputtering might convert some FeS_2 to FeS [16] indicated as a constant shoulder at 161 eV. Beyond a depth of 280 nm, sulfur decreases abruptly to give way to oxygen as also indicated by fig. 7. Fig. 6 shows a hydroxide species at an oxygen 1s binding energy of 532 eV [17] which vanishes after removal of less than 20 nm. Within the FeS_2 bulk, no oxygen exists until an oxide signal at 530.5 eV [17] becomes present mainly representing an iron oxide.
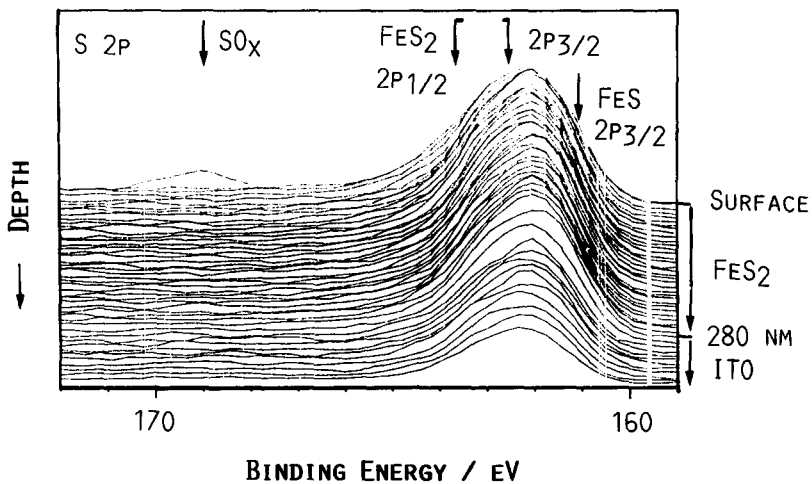
Fig. 5. Sulfur 2p XPS depth profile of a sulfurized sample on ITO after air contact at room temperature.

OXIDE

-OH

DEPTH

+ITO

280 NM

FeS$_2$

SURFACE

535   530

BINDING ENERGY / EV
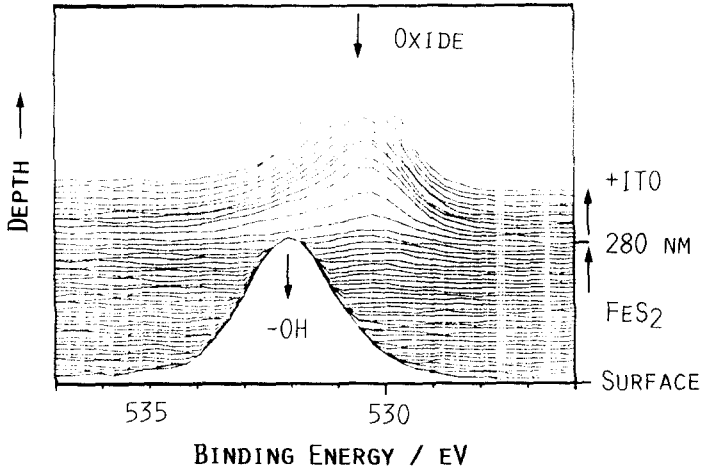
Fig. 6. Oxygen 1s XPS depth profile of sulfurized sample on ITO after air contact at room temperature.

A comparison of these sulfurized films with sprayed films [8] clearly indicates the superiority of the sulfurization technique. The profiling of a pinhole free area of a sprayed film indicates about 10 at% of oxygen throughout the bulk (fig. 8). We observe an average stoichiometry of $FeO_{0.3}S_{1.7}$. Fig. 9 shows oxygen 1s for this same sprayed film. This indicates hydroxide on the surface and oxide throughout the film. FeS itself is not detected in either the sulfurized or CSP films, but it can clearly be

DEPTH / NM

100   200   300

100

ATOM PERCENTS

S

FE

C   O   SN

500   1000   1500

SPUTTER TIME / S
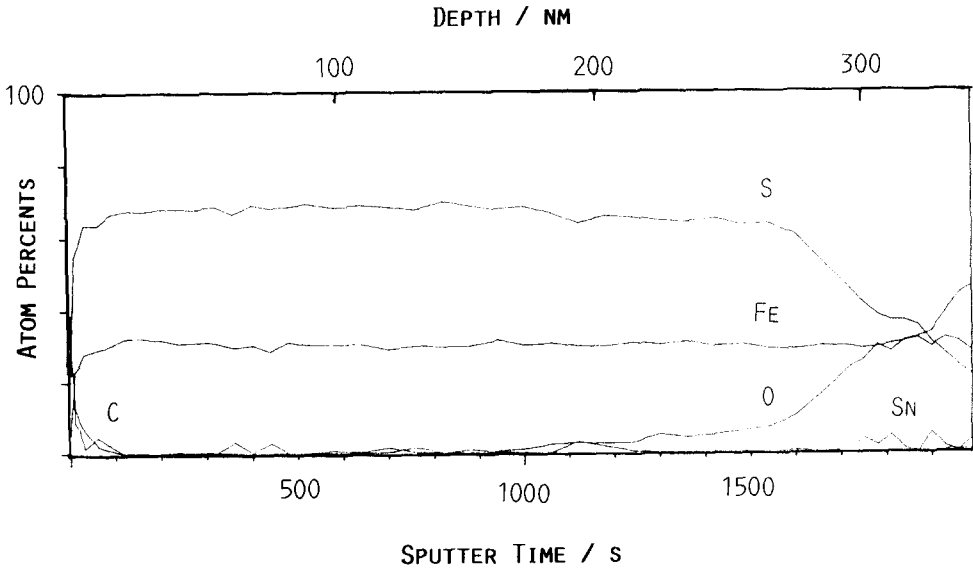
Fig. 7. Elemental XPS depth profile of sulfurized sample after air treatment at room temperature. The sulfur 2p, iron 2p, oxygen 1s, tin 2p and carbon 1s binding energies were used to create these plots.

DEPTH / NM
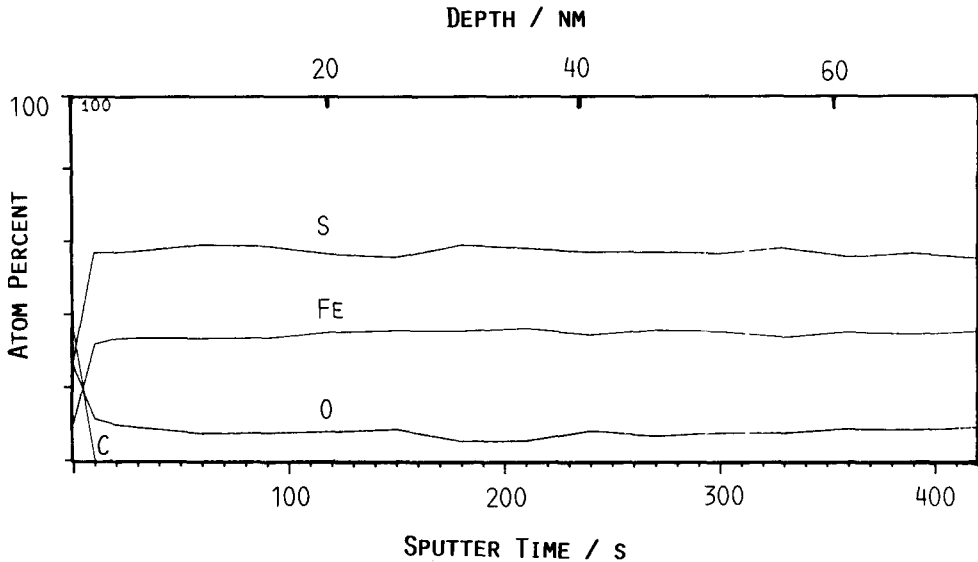
Fig. 8. Elemental XPS depth profile of a sprayed, CSP [8], sample after air contact at room temperature. The same binding energies were used as in fig. 7.

seen that the sulfurized films are of more ideal stoichiometry. A future publication will compare the morphology and composition of sprayed and sulfurized films.

3.2. Optical absorption

Figs. 10a–10c show representative plots of the optical absorption versus photon energy for film AE3. These plots are uncorrected for reflectance for the film surface,
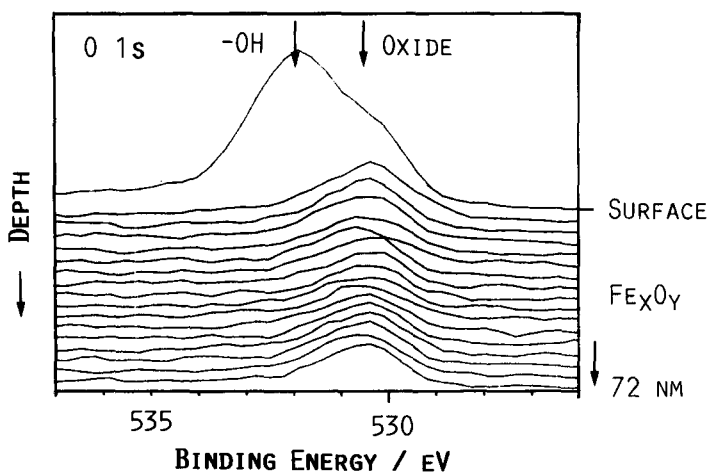
Fig. 9. Oxygen 1s XPS depth profile of the sprayed sample in fig. 8.

but yield results similar to previously obtained [8]. A pronounced absorption edge is seen near the vicinity of 0.9 eV. The plot for (absorption coefficient × photon energy)$^{0.5}$ in fig. 10b shows an indirect optical bandgap of 0.93 eV with a corresponding phonon energy of 0.16 eV [23,24]. Fig. 10c suggests a direct transition at 1.3 eV, but it is, as of yet, unclear as to the exact meaning of this result. Absorption tails in this polycrystalline material can be interpreted as band edge softening and Dow–Redfield (Urbach tail) effect [24,25].

3.3. Steady state and time resolved microwave conductivity

Photoconductivity (change in conductivity with applied light) measurements have been performed with the layers deposited on Kapton (AE3). The photoconductive spectrum normalized to photon flux at room temperature is shown in fig. 11. The onset of the photoconductivity occurs at 0.9 eV, and can be attributed to the band edge of pyrite. The two peaks near 1.1 and 1.3 eV might be interpreted as extrinsic photoconductivity, or may indicated two band transitions.
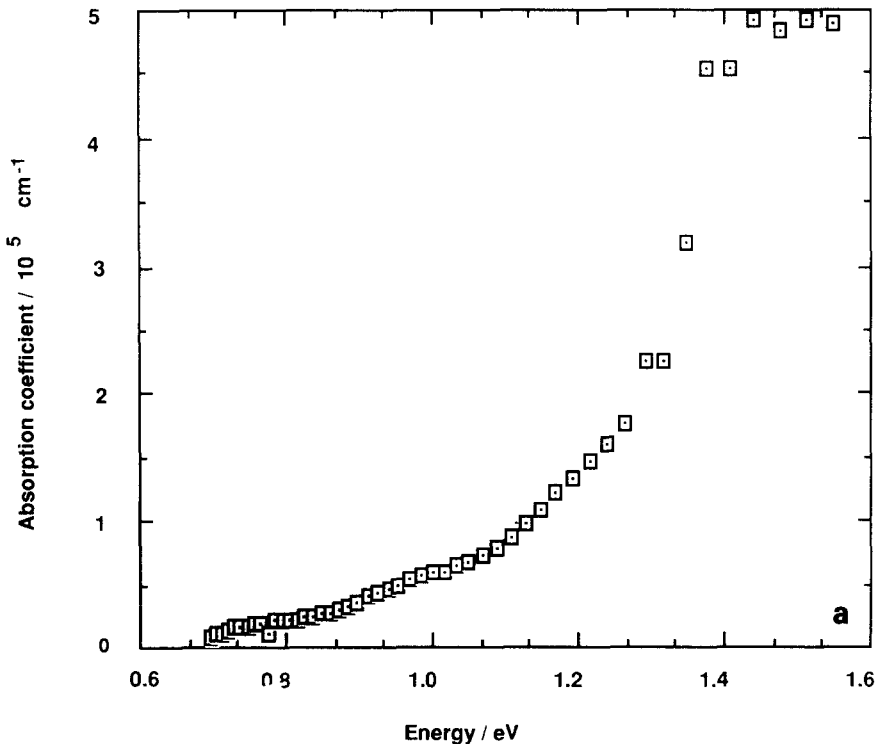
Fig. 10. (a) Optical absorption spectra of film AE3 data showing a high absorption coefficient (10^5 cm^{-1}), and (b) plotted as (absorption coefficient × photon energy)$^{0.5}$ showing possible indirect optical transition, and (c) (absorption coefficient × photon energy)^2 showing possible direct transition [24].
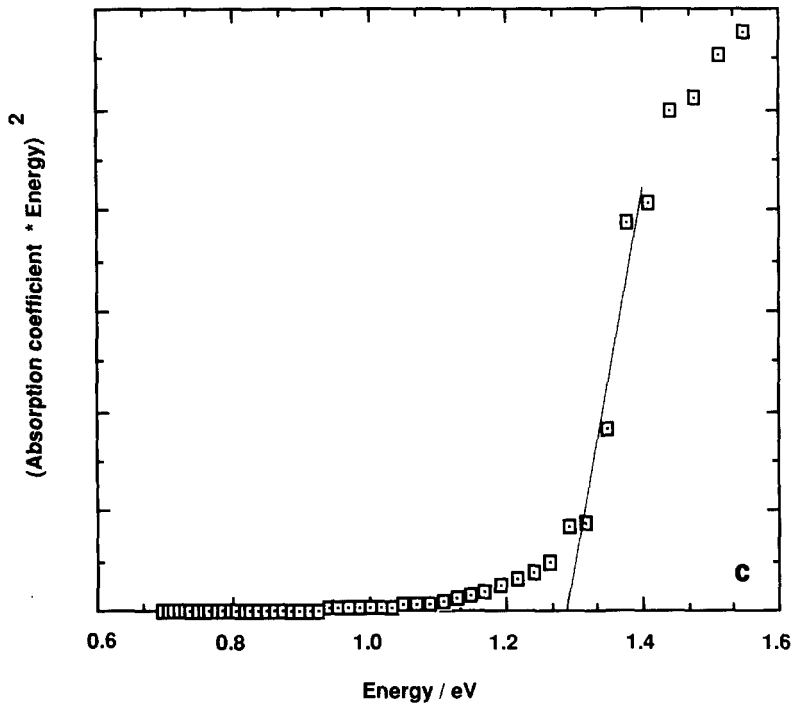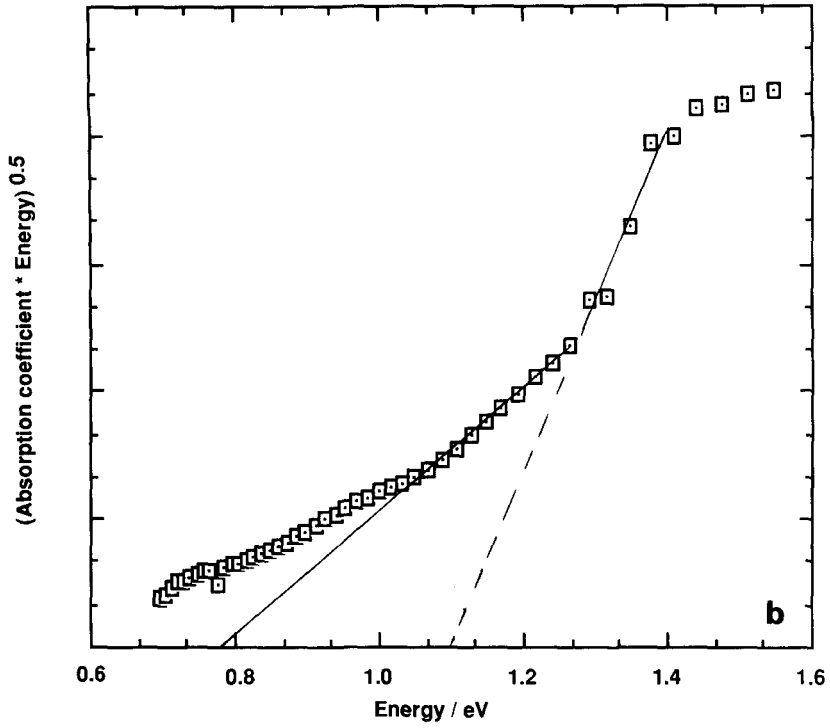
Fig. 10 (continued).
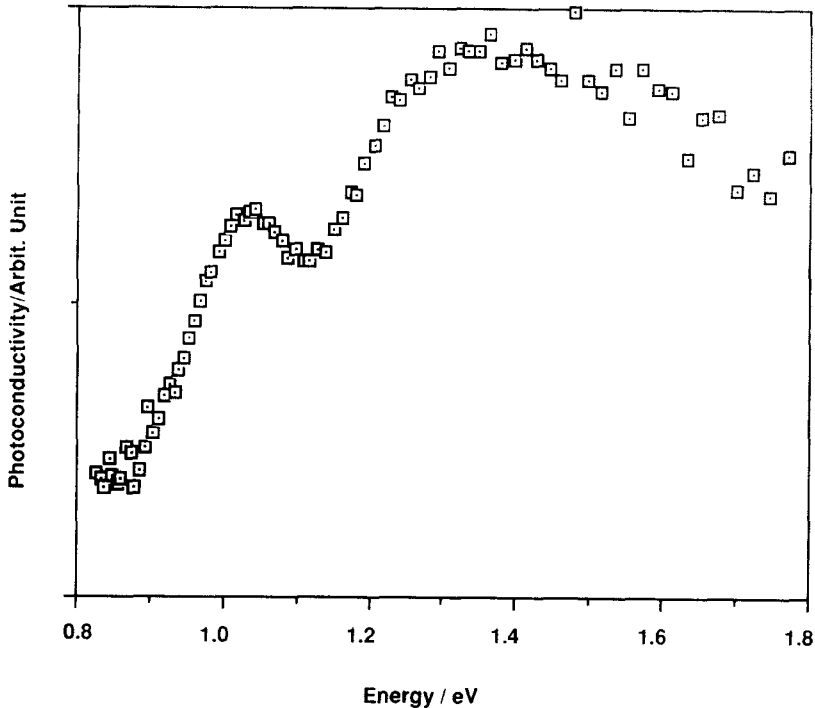
Fig. 11. Normalized photoconductivity plot versus photon energy at 300 K.

The dynamics of these free carriers within grains was detected by TRMC. The results are shown in figs. 12a and 12b. Comparing the lifetimes or decay times of the transient photoconductivity, a slightly longer time was found for an excitation wavelength of 1064 nm than for 532 nm. This can be explained in terms of the penetration depth of the light in the layer, which is about two orders of magnitude less in the case of the shorter wavelength light. The photogenerated carriers for the strongly absorbed 532 nm light recombine near the surface were the defect density is higher. Differences in absolute amplitude are due to the number of photogenerated carriers, which is a function of the incident photon flux, and is different for each wavelength used. These results, like the CSP results [8], show non-contact photore-sponse, but unlike the sprayed films, the next sections show that the sulfurized films can be used to produce a photovoltage.

3.4. Photoelectrochemical solar cell

A small cathodic photocurrent is produced for AE1 in contact with the iodide/ iodine redox couple (approximately 1 mV and 1 μA at AM 1.5 illumination). The polarity of this signal corresponds to a p-type semiconductor. This result is in agreement with the Seebeck or thermoelectric test. Fig. 13 shows the normalized quantum efficiency (electrons out per photon input) versus photon energy. Plots of
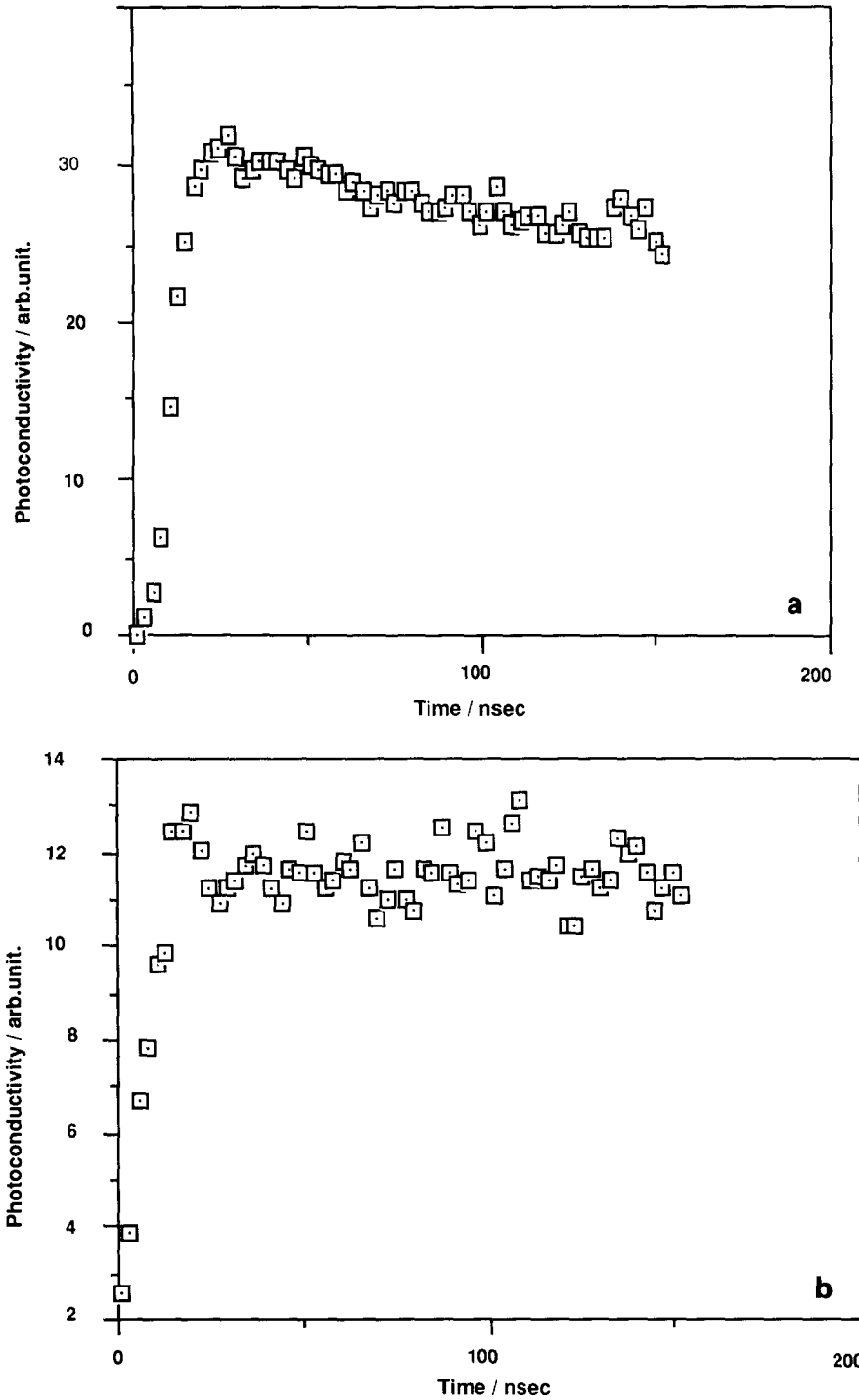
Fig. 12. TRMC for a pyrite film on Kapton film showing long decay times found in pyrite formed by sulfurization. Excitation wavelength (a) 530 nm, and (b) 1064 nm.
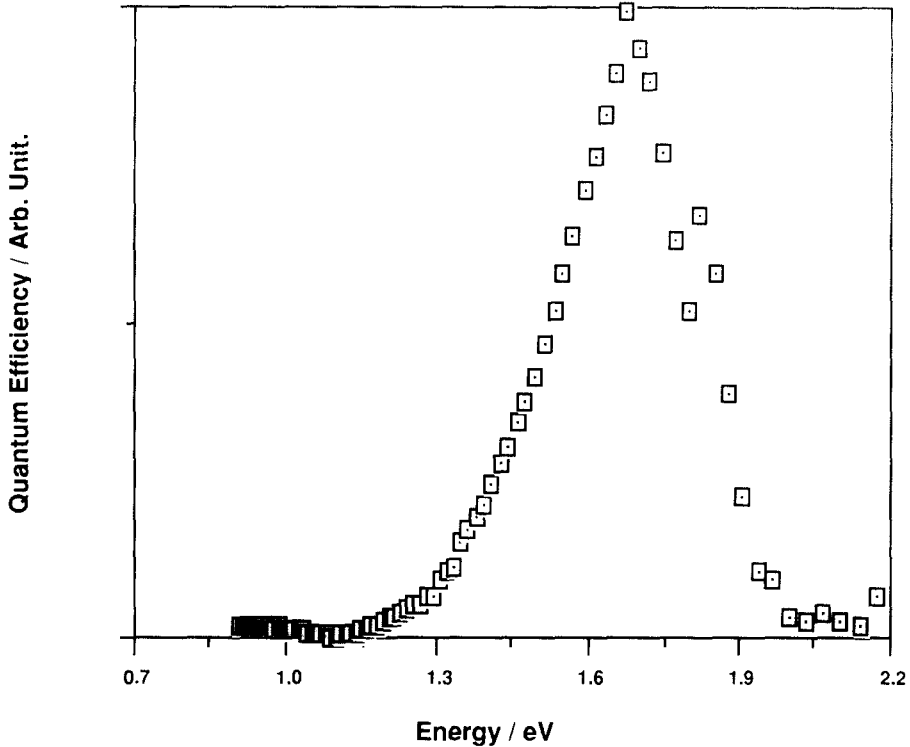
Fig. 13. Relative quantum efficiency (spectral response) of pyrite film on ITO glass (AE1) in an FeS_2/I^-, I_3^-/carbon photoelectrochemical solar cell configuration under short circuit conditions.

(quantum efficiency × photon energy)^n versus photon energy for $n = 0.5$ and 2, figs. 14a and 14b, suggest an indirect transition at 1.18 eV and a direct transition at 1.3 eV respectively. These values, although different than the results of the optical absorption, are consistent with those of pyrite if one considers that the dependency of quantum efficiency on absorption coefficient is not linear unless the absorption coefficient diffusion length product is small.

4. Discussion

The previous sections have indicated that the pyrite films prepared by sulfurization show good material properties and purity, yet only small photocurrents and voltages are observed in an photoelectrochemical solar cell. There are three possible reasons for this that are currently being investigated. The first is that pyrite grains in the polycrystalline film may be oriented in such a way that many grain boundaries must be traversed by an electron from the bottom contact to the top interface. Preliminary SEM analysis shows that this may be the case. Columnar grains are more desirable, since the photogenerated carriers are confined to only one grain
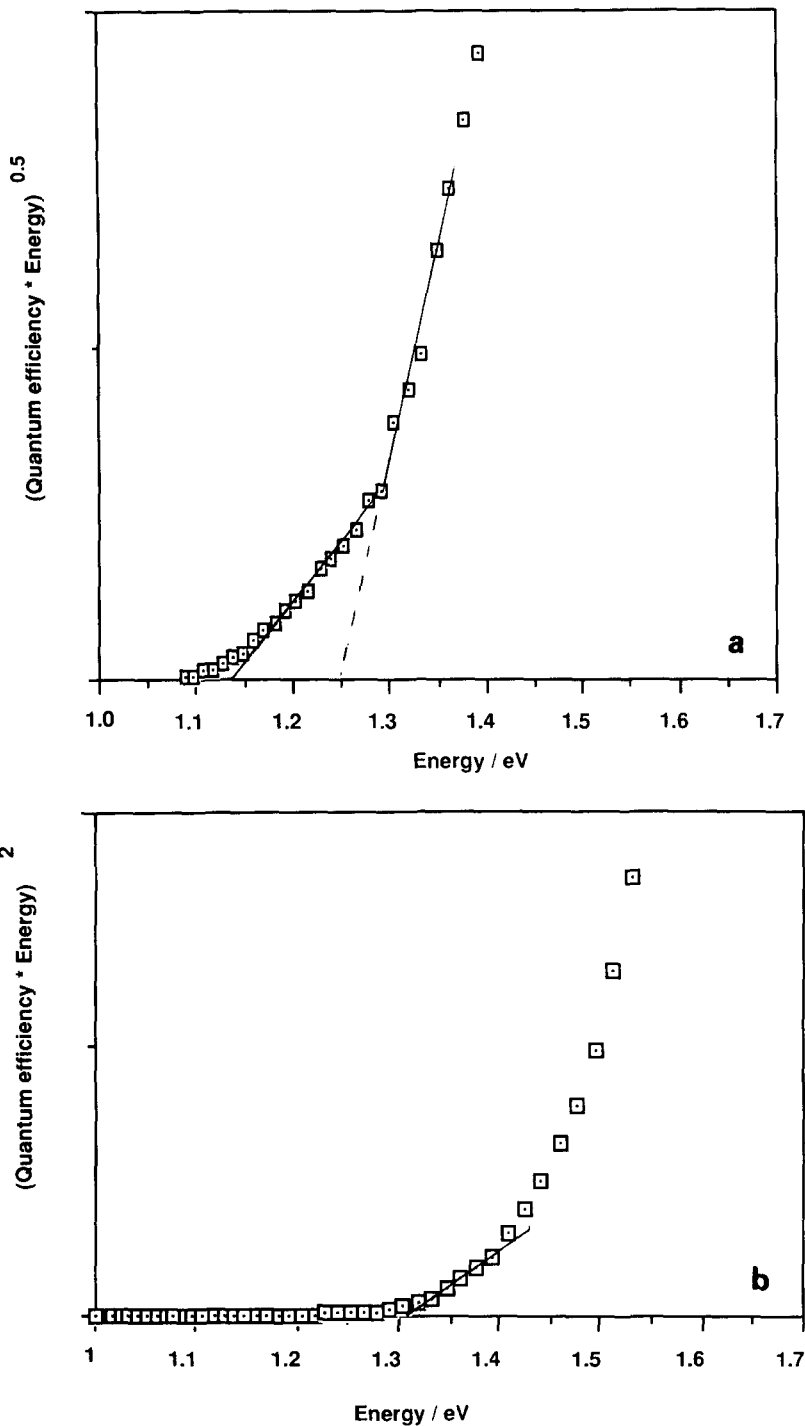
Fig. 14. (a) Plot of (quantum efficiency × photon energy)$^{0.5}$ versus photon energy, and (b) plot of (quantum efficiency × photon energy)^2 versus photon energy for the photoelectrochemical solar cell.

boundary before collection [24]. Experiments are currently being conducted to orient the grains by recrystallization both before or after sulfurization. The second reason for poor response may lie in the presence of micro-pinholes [8]. The presence of pinholes in the pyrite layer may lead to a short circuit in the photogenerated current and effectively shunt the pyrite solar cell. Experiments are currently being conducted involving the application of a negative photoresist to the ITO/pyrite film. Subsequent exposure of this polymer to UV radiation through the ITO layer will cure and harden the photoresist, and form a insulating barrier on the conductive ITO layer where a pinhole is present. The last reason for poor response is a simple one. The electrolyte solution used to form the electrochemical Schottky barrier has been optimized for n-type material [2,3]. The barrier heights and Fermi levels are not optimized for the p-type material found here. Future experiments will modify the electrolyte solution for the electrochemical solar cells, and concentrate on the development of suitable window layer materials for conventional solid state cells.

5. Conclusions

Photoactive semiconducting FeS_2 (pyrite) films can be prepared by conversion of iron oxide films with gaseous sulfur at 350°C. As predicted by the interpretation of the Fe–O–S phase diagram, the layers do not contain FeS and are of good stoichiometry. They exhibit p-type conductivity as shown by preliminary photoelectrochemical measurements. Best results to date have been obtained using Dupont Kapton foil as a substrate. This configuration and method, if proven efficient in a photovoltaic or photoelectrochemical cell, could provide economical "roll to roll" solar cells and give fool's gold a great worth in a world now looking for alternatives to fossil fuels.

Acknowledgements

References

[1] A. Ennaoui, S. Fiechter, H. Goslowsky and H. Tributsch, J. Electrochem. Soc. 132 (1985) 1579.
[2] A. Ennaoui, S. Fiechter, W. Jaegerman and H. Tributsch, J. Electrochem. Soc. 133 (1986) 97.
[3] A. Ennaoui and H. Tributsch, Sol. Energy Mater. 14 (1986) 461.
[4] R. Schieck, A. Hartman and S. Fiechter, J. Mater. Res., submitted.
[5] A. Ennaoui and H. Tributsch, J. Electroanal. Chem. 204 (1986) 185.
[6] S. Fiechter, J. Mai, A. Ennaoui and W. Szacki, J. Cryst. Growth 78 (1986) 438.

[7] G. Chatzitheodorou, S. Fiechter, R. Konenkamp, M. Kunst, W. Jaegerman and H. Tributsch, Mater. Res. Bull. 21 (1986) 1481.

[8] G. Smestad, A. da Silva, H. Tributsch and S. Fiechter, Sol. Energy Mater. 18 (1989) 299.

[9] G. Kullerud, Carnegie Inst. Washington Annu. Rep. Div. Geophys. Lab. 56 (1957) 198.

[10] E.R. Cohen and B.N. Taylor, Phys. Today BG (1989) 8-8d.

[11] P. Scherrer, Nachr. Göttinger Ges. 2 (1918) 98.

[12] H.P. Kung and L.E. Alexander, X-ray Diffraction Procedures (Wiley, New York, 1974).

[13] Siemens Application Note No. 75 (Siemens Energy and Automation, Cherry Hill, NJ, 1984).

[14] M. Kunst and H. Tributsch, Chem. Phys. Lett. 105 (1984) 123.

[15] M. Kunst and G. Beck, J. Appl. Phys. 60 (1986) 3558.

[16] Phoenicon Photoactive Systems GmbH, Bismarckstrasse 58, D-1000 Berlin 12, Germany.

[17] C.D. Wagner, W.M. Riggs, L.E. Davis and J.F. Moulder, in: Handbook of X-Ray Photoelectron Spectroscopy, Ed. G.E. Muilenberg (Perkin Elmer, Eden Prairie, MN, 1978).

[18] H. van der Heide, R. Hemmel, C.F. van Bruggen and C. Haas, J. Solid State Chem. 33 (1980) 17.

[19] C. Pettenkofer, in: Proc. 5th Latin American Symp. on Surface Physics, CIF Series Vol. 11, Eds. M. Cardona and J. Giraldo (World Scientific, Singapore, 1988) p. 243.

[20] H. Binder, Z. Naturforsch. 28b (1973) 255.

[21] L.N. Kramer and M.P. Klein, J. Chem. Phys. 51 (1969) 3618.

[22] A. Buckley and R. Woods, Appl. Surf. Sci. 27 (1987) 437.

[23] F. Stern, Solid State Phys. 15 (1963) 299.

[24] A. Fahrenbruch and R. Bube, Fundamentals of Solar Cells (Academic Press, New York, 1983).

[25] J. Dow and D. Redfield, Phys. Rev. B 1 (1970) 3358.